PCCP

ROYAL SOCIETY OF CHEMISTRY

PAPER

View Article Online
View Journal | View Issue



Cite this: *Phys. Chem. Chem. Phys.*, 2024, **26**, 22611

# Pathways of cluster growth: infra-red multi-photon dissociation spectroscopy of a series of Re–Si clusters, $[ReSi_n]^+$, $n$ = 3–9†

Roshan Singh, *[a] PieterJan Claes,[b] André Fielicke,[c] Ewald Janssens,[b] Peter Lievens[b] and John E. McGrady[a]

Received 29th May 2024,
Accepted 8th August 2024

DOI: 10.1039/d4cp02208d

rsc.li/pccp

Infra-red multiple-photon dissociation spectroscopy on Xe-tagged Re/Si clusters, $[ReSi_n]^+$, $n$ = 3–9, reveals intense absorption features around 400 $cm^{-1}$, along with, in some cases, additional bands in the 250–350 $cm^{-1}$ window. A survey of the potential energy surface using density functional theory in conjunction with particle swarm optimisation indicates a growth pattern based on a growing network of Si atoms wrapped around the Re centre: the $Si_n$ units can be viewed as fragments of a putative 16-vertex Frank–Kasper polyhedron. The structural evolution for the $[ReSi_n]^+$ series differs significantly from the iso-electronic Mn series studied previously, where the metal ion is typically bound externally to the surface of a growing 3-dimensional $Si_n$ cluster, the differences reflecting the greater accessibility of 5d *vs.* 3d electron density.



## Introduction

Over the past several decades, many different models that aim to reconcile the structure of main-group clusters with their valence electron count have emerged. Amongst these, electronic shell models have been applied with much success to s-block metals[1] while the Wade–Mingos rules[2,3] and their extension by Jemmis and co-workers[4] have brought order to the remarkably diverse structural chemistry of the borane family. Jemmis' rules address a critically important question in cluster chemistry: how do they grow? The idea that clusters can be constructed from smaller building blocks (a single polyhedron in the context of Jemmis' rules) is an attractive one, and, if the principles that control coalescence can be established, it opens up a route to the custom synthesis of clusters of different size and composition.[5]

X-Ray crystallography has been the tool of choice to explore the structures of clusters in the inorganic domain, most prominently in the context of Zintl-ion chemistry.[6,7] For the large majority of cluster species that are not amenable to crystallisation, however, a range of gas-phase techniques including infra-red multi-photon dissociation (IR-MPD),[8–11] photoelectron[12–16] and X-ray absorption[17] spectroscopies, typically complemented by density functional theory, can provide structural insight, albeit in a less direct manner. Of particular relevance to the present work is a series of papers discussing the structure of manganese/Si clusters, $[MnSi_n]^{0/+}$. In 2012, Ngan and co-workers reported the IR-MPD spectra of the cationic family, $[MnSi_n]^+$, $n$ = 6–14.[10] By matching the measured spectra to the DFT-computed fingerprint of candidate structures, the authors established quite different growth patterns for small and large clusters. For $n$ = 6–10, a manganese ion is bound exohedrally to an expanding Si cluster, and the low coordination numbers lead to high multiplicities: quintets for $n$ = 6 and 8–10 and a septet for $n$ = 7. In contrast, clusters with $n > 11$ adopt fullerene-like geometries with the manganese centre encapsulated inside the cluster, with the higher coordination numbers leading to singlet or triplet ground states.[18–20] The spectra of the neutral analogues of the smaller clusters, $MnSi_n$, $n$ = 6–9, are very similar to those of the cations, as are their characteristically high magnetic moments (sextets for $n$ = 6, 8, 9, a quartet for $n$ = 7).[21] The intimate connection between magnetic moment and endohedral encapsulation in $[MnSi_n]^+$ was confirmed independently by Zamudio-Bayer *et al.* using X-ray magnetic circular dichroism (XMCD),[17] which indicates the presence of a local magnetic moment on the manganese atom for $n$ = 7–10, but not for the larger clusters.

[a] *Department of Chemistry, University of Oxford, South Parks Road, Oxford OX1 3QR, UK. E-mail: john.mcgrady@chem.ox.ac.uk*
[b] *Quantum Solid-State Physics, Department of Physics and Astronomy, KU Leuven, Celestijnenlaan 200 D, B-3001 Leuven, Belgium. E-mail: ewald.janssens@kuleuven.be*
[c] *Fritz-Haber-Institut der Max-Planck-Gesellschaft, Faradayweg 4-6, 14195 Berlin, Germany. E-mail: fielicke@fhi-berlin.mpg.de*

† Electronic supplementary information (ESI) available: Further details of experiments on $[ReSi_4]^+$ and discussion of the influence of the Xe tag on the computed spectra. List of cartesian coordinates of all reported minima and animated gifs of significant vibrational modes. See DOI: https://doi.org/10.1039/d4cp02208d

In this paper, we turn our attention from the lightest member of group VII, Mn, to its heaviest congener, Re, and IR-MPD spectroscopy to explore growth patterns in the series $[ReSi_n]^+$, $n$ = 3–9. Hiura and co-workers have previously shown that reaction of gas-phase $Re^+$ with $SiH_4$ generates a series of $[ReSi_n]^+$ clusters, amongst which the $n$ = 11 was particularly abundant.[22] Han's subsequent DFT studies on neutral $ReSi_n$ suggest that a transition from exohedral to endohedral coordination of the Re ion occurs at $n$ = 8.[23] Vertical trends in the d block suggest that states with lower multiplicity should prevail in Re, and also that higher oxidation states should be rather more accessible. These electronic factors, along with the larger radius of Re, offer up the possibility of quite different growth patterns in the isoelectronic $[MnSi_n]^+$ and $[ReSi_n]^+$ series. By monitoring the changes in the vibrational spectra as a function of size and comparing them to computed spectra of candidate structures, we aim to build a model of cluster growth and show how the different properties of the transition metals influence the growth of Si networks around them.

# Methodology

### Experimental techniques

All spectroscopic measurements are performed in a molecular beam set up[8] coupled to a beamline of the free electron laser for infrared experiments (FELIX) user facility.[24] The clusters are produced in a dual-target dual-laser vaporization cluster source by pulsed ablation of Re and Si plate targets.[25] Cluster-xenon complexes are formed by condensation of the vaporized material in a short pulse of He gas containing a fraction of isotopically enriched $^{129}Xe$ and cooled in a thermalization channel attached to the source. Resonant absorption of IR light heats the cluster-xenon complexes through internal vibrational redistribution, which may result in dissociation of the complex. Infrared multiple photon dissociation (IR-MPD) spectra are constructed by recording the intensities of the ionic complexes as a function of the FELIX frequency in the 225 to 600 $cm^{-1}$ range using a time-of-flight mass spectrometer. From these depletion measurements, relative absorption cross sections are determined as described previously.[8] The FELIX laser output consists of 5–8 μs macropulses with a typical energy of 50 mJ and a bandwidth of 3–4 $cm^{-1}$. The resonant absorption of infrared light is reflected by the fragmentation of the xenon messenger atoms and thus the simultaneous decrease of $[ReSi_n{\cdot}Xe]^+$ and increase of $[ReSi_n]^+$ intensities in the mass spectra. The IR spectrum of the cluster is then obtained by plotting the intensity:

$$I = -\frac{1}{P_\nu}\ln\left(\frac{I_\nu}{I_0}\right) \quad (1)$$

with $P_\nu$ the wavelength dependent laser energy, and $I_\nu$ and $I_0$ the intensity of $[ReSi_n{\cdot}Xe]^+$ in the mass spectrum with and without laser excitation, respectively. Note that the negative sign in eqn (1) means that a reduction in intensity of $[ReSi_n{\cdot}Xe]^+$ $\left(\frac{I_\nu}{I_0} < 1\right)$ corresponds to a positive peak (an enhancement) in the corresponding spectrum.

### Computational techniques

We have surveyed the potential energy surfaces of the $[ReSi_n]^+$ clusters using particle-swarm optimisation (PSO) as implemented in the CALYPSO package, version 7.[26] The particle-swarm approach has been used extensively for cluster structure prediction,[27] and relies on generation of a population of candidate solutions. The structures are then adapted by changing atomic positions, guided by the best solution of the candidate itself, but also by the best known solution of the entire population. CALYPSO provides a local version of PSO allowing for an investigation of complex potential energy surfaces (PES) by segmenting the PES and performing multiple PSO calculations. This local PSO scheme is utilised for all the cluster sizes. Two separate calculations were performed involving different fractions, 60% and 80%, of structures generated through PSO and the remainder randomly generated to increase the diversity of the population.[26] These randomly generated structures were first optimised using the PBE functional[28] in conjunction with the LanL2DZ basis set[29] in Gaussian 09, revision D.01.[30] before being used as the initial population for the PSO calculations. The 50 lowest energy structures generated by the PSO approach were then optimised using the PBE functional and a Slater-type triple-zeta basis set with two polarisation functions (TZ2P)[31] in the Amsterdam density functional (ADF) package, version 2021.104.[32] The density was fitted using the QZ4P set of fit functions and a "good" quality Becke grid was used throughout for the numerical integration. The PBE functional has been used extensively in computational cluster chemistry, including in our own previous work on $[MnSi_{12}]^+$ and $[Mn_2Si_n]^+$, $n$ = 10, 11, 12.[33] Once the octahedral structure of $[ReSi_5]^+$ was identified as a common structural component of the larger clusters, the unbiased PSO procedure was complemented with a systematic survey of all possible orientations of capping atoms over the different faces of the octahedral core. This yielded a number of new local minima which were not present in the original population, but none proved to be more stable than those identified by PSO. Harmonic vibrational frequencies were computed at the equilibrium geometries using the same combination of functional and basis set, with each resonance broadened into a Lorentzian line shape of 10 $cm^{-1}$ full width at half maximum in the figures.[33] In all computed spectra reported here, the frequencies are unscaled. The similarity between simulated and experimental infrared spectra can be quantified using the cosine similarity (CS) score:[34,35]

$$\mathrm{CS} = \cos(\theta) = \frac{\mathbf{a}\cdot\mathbf{b}}{\|\mathbf{a}\|\|\mathbf{b}\|} \quad (2)$$

where $a$ and $b$ are two $n$-dimensional vectors with elements $a_i$ and $b_i$ which represent the measured and computed intensities at a given frequency, respectively. Values of CS lie between 0 and 1, with larger numbers indicating a better match.[34] In the following discussion, the CS is used only in cases where there are multiple well-defined peaks in the experimental spectrum.

 

## Results and discussion

### Mass spectrometry

The mass spectrum of $^{129}$Xe complexes of the Re-doped clusters, measured at 130 K with 1.5% Xe in the He carrier gas, is shown in Fig. 1. Re has two isotopes $^{185}$Re and $^{187}$Re in the ratio 37.4 : 62.6 and the mass of the lighter isotope coincides with that of a $Si_2$. $^{129}$Xe fragment, so the presence of the Re clusters was identified using only the peak corresponding to the heavier $^{187}$Re isotope. Single Re doped Si clusters, $[ReSi_n]^+$, are observed for $n$ = 5–14 (red lines) and their Xe-tagged analogues, $[ReSi_n]^+\cdot Xe$, for $n$ = 3–9 (blue lines). Double-tagged complexes, $[ReSi_n]^+\cdot Xe_2$, marked by asterisks in Fig. 1, are also present in low concentrations for the smallest clusters ($n$ = 1–4).

### IR-MPD spectroscopy of $[ReSi_{3-9}]^+$ and comparison to $[MnSi_{6-9}]^+$

The IR-MPD spectra of the cationic clusters $[ReSi_n]^+$, $n$ = 3–9, are collected in Fig. 2. The spectra are measured on the mono-tagged Xe complexes, $[ReSi_n]^+\cdot Xe$, with the exception of $[ReSi_4]^+$ where the doubly tagged cluster, $[ReSi_4]^+\cdot Xe_2$, was used (*vide infra*). The spectra of $[ReSi_3]^+$ and $[ReSi_5]^+$ appear particularly simple, with only a single prominent peak, at 430 and 380 cm$^{-1}$, respectively. In contrast the $[ReSi_4]^+$ spectrum has an intense feature at lower frequency, 340 cm$^{-1}$, along with two smaller absorption bands between 400 and 450 cm$^{-1}$. There is also evidence for an intense peak at the lower limit of the spectrum, around 230 cm$^{-1}$. The larger clusters, from $[ReSi_6]^+$ up to $[ReSi_9]^+$, are similar in so far as they have features around 300 cm$^{-1}$ in addition to the characteristic broad and intense peak between 380 and 430 cm$^{-1}$. The spectra of $[ReSi_n]^+$ differ significantly from their Mn analogues, first reported in Fig. 2 of ref. 10 and reproduced below in Fig. 3. The spectra of the Mn clusters typically have a larger number of well-resolved bands that are, in some cases, located above 450 cm$^{-1}$, considerably higher than any of those in $[ReSi_n]^+$. Complementary DFT calculations on the Mn-based clusters indicated a growth pattern based on a Mn atom/ion bound rather weakly and exohedrally to an expanding and approximately spherical $Si_n$ unit.[10] Based on this first reading of the spectra, we will separate our computational analysis into two separate sections, the first dealing with growth patterns in the smaller clusters, $[ReSi_3]^+ \rightarrow [ReSi_5]^+$, and the second with the larger clusters, $[ReSi_6]^+ \rightarrow [ReSi_9]^+$. We will then return to a comparison of Mn and Re in light of the computational results.

### Early stages of growth: $[ReSi_{3-5}]^+$

For the three smallest clusters, we have performed a detailed analysis of the singlet, triplet and quintet potential energy surfaces following the protocol set out in the computational methods section. Full details are presented in ESI,† but it suffices here to note that all non-singlet states were found to be more than 0.9 eV above the singlet global minimum, and will not be considered further. This represents an immediate contrast to $[MnSi_n]^+$ where the exohedrally doped ($n < 10$) clusters have a local magnetic moment on Mn.[10,17] The optimised structures of the global minima are shown in Fig. 4, where a second low-lying isomer of $[ReSi_5]^+$ is also included.

The singlet ground state of $[ReSi_3]^+$ has $C_{3v}$ symmetry, with a triangular $Si_3$ unit, and the computed spectrum features an intense *e*-symmetric combination of Re–Si stretches at 431 cm$^{-1}$, in excellent agreement with the single intense band in the IR-MPD spectrum. The totally-symmetric $a_1$ combination of Re–Si stretches appears as a low-intensity band at 496 cm$^{-1}$ which may map on to a weak feature around 485 cm$^{-1}$ in the experimental spectrum, although the low signal-to-noise ratio in this region precludes a definitive assignment. The most stable isomer of $[ReSi_5]^+$, $^1$5$^+$(*a*), is also highly symmetric ($C_{4v}$) and, as a result, also has a relatively simple vibrational spectrum. The structure is based on a square pyramidal $Si_5$ unit with the Re atom capping the square face, and the spectrum is dominated by a single *e*-symmetric mode at 387 cm$^{-1}$, again a linear combination of Re–Si stretches. The $a_1$-symmetric combination of Re–Si stretches computed at 434 cm$^{-1}$ is dipole-allowed but has very low intensity, while the $a_2$-symmetric

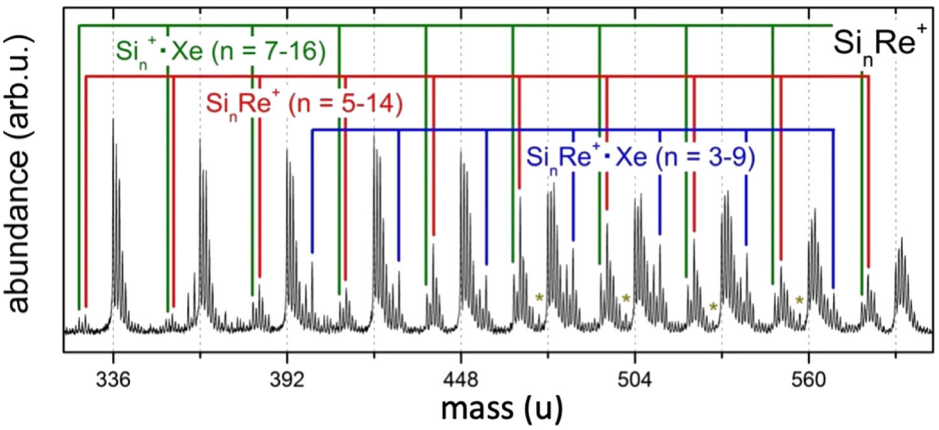


Fig. 1 Mass spectrum of Re doped Si clusters produced with the source at 130 K and 1.5% Xe in He mixture for the carrier gas. The four small peaks marked with asterisks at 473 u, 501 u, 529 u and 557 u correspond to the most abundant isotopes of the doubly tagged clusters $[ReSi_n]^+\cdot Xe_2$, $n$ = 1–4. The intense peaks at 336, 364, 392, 420, 448, 476, 504, 532, 560 and 588 (marked by dashed lines) correspond to the lightest isotopomers of the bare silicon clusters $Si_{12-21}^+$.

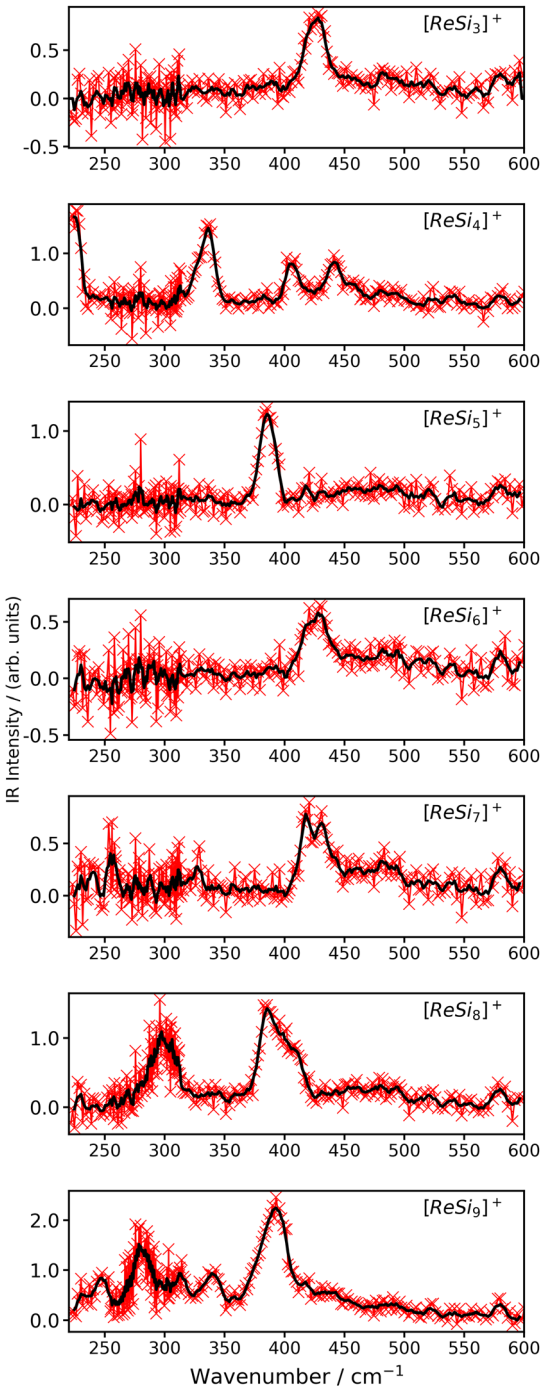


Fig. 2 IR-MPD spectra of $[ReSi_n]^+$, $n$ = 3–9. The spectra are measured using the mono-tagged adducts $[ReSi_n]^+$·Xe for all clusters other than $[ReSi_4]^+$, where the double adduct $[ReSi_n]^+$·$Xe_2$ is used.

combination at 342 $cm^{-1}$ is dipole forbidden: there is no obvious peak corresponding to either in the measured spectrum. A second $a_1$-symmetric mode at 228 $cm^{-1}$ does, however, have high intensity: this mode corresponds to the dissociation of the cluster into separate Re and $Si_5$ units. Nevertheless, there is again no corresponding feature in the experimental spectrum. The peak is very close to the lower limit of the experimental range, so one possible explanation for its absence is

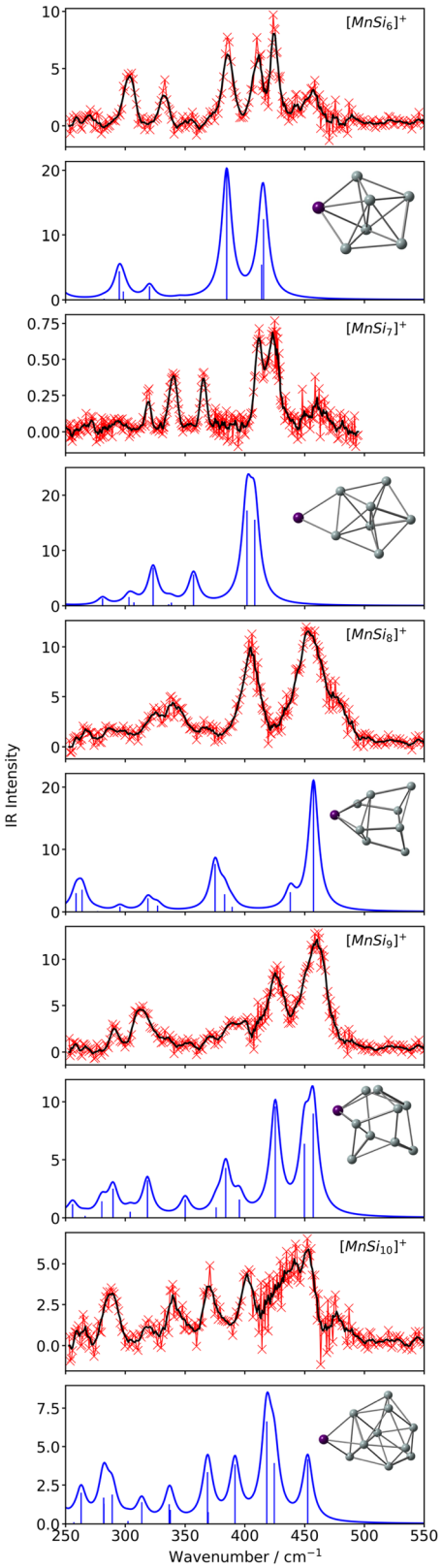


Fig. 3 IR-MPD spectra of $[MnSi_n]^+$, $n$ = 6–10. The spectra have been calculated using the geometries reported in ref. 10, but using the same computational protocol adopted for the other calculations in this work (ADF, PBE/TZ2P). Intensity is given in arbitrary units for the measured spectra, and km $mol^{-1}$ for the computed spectra.

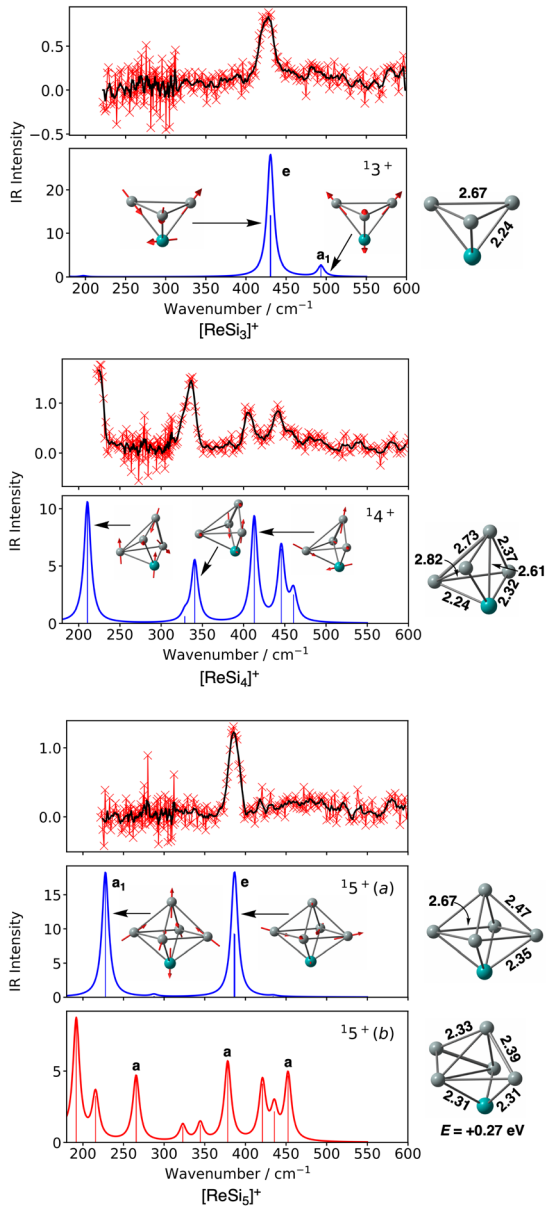


Fig. 4 IR-MPD spectra of $[ReSi_{3-5}]^+$, along with DFT-optimised structures of the singlet ground states and simulated vibrational spectra. Bond lengths are shown in units of Å. Intensity in arbitrary units for the measured spectra, and km mol$^{-1}$ for the computed spectra.

that it lies just beyond the limits of detection. However, this appears to be a general feature of these clusters: we also compute modes with similar frequencies and intensities and amplitudes (*i.e.* dissociation into Re and Si$_n$) for $[ReSi_6]^+$ and $[ReSi_7]^+$ (*vide infra*), neither of which is matched by an obvious feature in the experimental spectrum. This suggests that there is some systematic error in the computed frequency or intensity of modes of this type. In an attempt to resolve this question, we have considered the possible role of the Xe tag (or lack thereof) in our computational model, an issue that has been addressed in some detail in the context of the manganese clusters by Ngan *et al.*[36] who observed that Ar binds strongly to $[MnSi_n]^+$, $n$ = 6, 8–10 but not to $[MnSi_7]^+$.[10] The presence of a rare gas atom does not typically perturb the IR-MPD spectra of silicon clusters to any great extent,[9] and similar observations have been made in the context of $[Rh_5Ta(NO)]^+$ by Mafuné and co-workers.[37] In metal-oxide clusters such as $[Pt_2O_3]^+$, however, the effects of binding of an Ar atom can be far from negligible, even changing the energetic order of the isomers.[38] The computed frequencies and intensities shown in Fig. 4 relate to vibrations of the bare $[ReSi_n]^+$ clusters, but if the Xe tag is included explicitly in the model (where it is found to bind to the Re centre), the intensity of the low-frequency (228 cm$^{-1}$) band is significantly reduced (ESI,† Fig. S3). In contrast, the Xe tag has minimal impact on any of the vibrational modes above 250 cm$^{-1}$, where the motion of the Re atom is less pronounced.‡ The neglect of the Xe tag in the computational model appears, therefore, to lead to a systematic overestimation of the intensity of the Re–(Si$_n$) stretching mode relative to all others. The perturbation induced by the tag is less pronounced in the larger clusters, where the Re atom is encapsulated more strongly by the growing Si$_n$ network.

For the previous two examples, the depletion of the intensity of the $[ReSi_3]^+$·Xe and $[ReSi_5]^+$·Xe peaks was used to probe the infra-red absorption. When the intensity of the $[ReSi_4]^+$·Xe peak is used in the same way, however, an increase in intensity is observed at 220 cm$^{-1}$, 333 cm$^{-1}$, 404 cm$^{-1}$ and 440 cm$^{-1}$ (see ESI,† Fig. S1). The most likely source of this increase is that the doubly tagged cluster, $[ReSi_4]^+$·Xe$_2$, the small peak marked by an asterisk in the mass spectrum at 557 u, is decomposing *via* loss of Xe, replenishing the peak due to $[ReSi_4]^+$·Xe. We have, therefore, used the intensity of the doubly tagged species, which shows the normal reduction at the same set of frequencies, to generate the spectrum that is shown in Fig. 2 and 4. The vibrational spectrum of the $[ReSi_4]^+$ cluster is considerably richer than either $[ReSi_3]^+$ or $[ReSi_5]^+$, and the larger number of bands immediately flags a less symmetric geometry. The $C_s$-symmetric optimised structure shown in Fig. 4 can be considered as a ReSi$_3$ square with short Re–Si and Si–Si bond lengths of 2.32 and 2.37 Å, respectively. The fourth Si atom is then strongly bound to the Re (2.24 Å) but rather more weakly to the other three Si atoms (2.73 and 2.82 Å). The presence of an 'isolated' Si atom, bound strongly to Re but only weakly to all other Si centres, is a unique feature of $[ReSi_4]^+$ that sets it apart from all other clusters studied here. The low-frequency region of the spectrum is dominated by an intense band near 350 cm$^{-1}$ which corresponds to an out-of-phase combination of Re–Si stretching modes in the ReSi$_3$ base. At 410 cm$^{-1}$ a second intense band corresponds to the stretch of the very short Re–Si bond. The $[ReSi_4]^+$ cluster is also unique from a spectroscopic perspective in so much as it has an intense band at the extreme lower limit of detection, at 225 cm$^{-1}$. The computed spectrum contains a band at 211 cm$^{-1}$ that corresponds to a Si–Si stretching mode, localised along the long Si–Si bond of 2.73 Å: this mode is quite distinct from the Re–(Si$_n$) stretches noted in the previous paragraph, and indeed

‡ This observation is not an artifact of the choice of functional – it is also observed in calculations performed with the hybrids PBE0 and B3LYP.

its intensity is not substantially reduced even when the Xe tag is included in the computational model. This feature appears, therefore, to signal the presence of an isolated Si atom, only weakly bound to the other Si atoms of the cluster.

### Later stages of growth: $[ReSi_{6-9}]^+$

Starting from the octahedral core of $[ReSi_5]^+$, the optimised structures of the larger clusters, $[ReSi_{6-9}]^+$, can all be understood in terms of a systematic growth pattern based on capping of triangular faces. For the $[ReSi_6]^+$ cluster, we can identify three distinct isomers, $^1$6$^+$(*a*), (*b*) and (*c*) in Fig. 5. The most stable, $^1$6$^+$(*a*), is derived by capping a $Si_3$ face of the octahedron while $^1$6$^+$(*b*), in contrast, has the sixth Si atom capping an $ReSi_2$ face. $^1$6$^+$(*c*) has a chair-like $Si_6$ unit with the Re coordinated to one face. The three isomers are separated by only 0.17 eV, too close to allow a confident assignment of the equilibrium structure based on relative energy alone. Turning to the comparison between computed and experimental spectra, all three isomers have an intense peak in the same window as the experimental feature at 430 cm$^{-1}$, although it is somewhat lower in $^1$6$^+$(*c*). The experimental spectrum is noisy in the region below 300 cm$^{-1}$, so the differences in the computed spectra in this part of the spectrum are less useful as a diagnostic tool. We can attempt to quantify the similarity between computed and measured spectra using the cosine similarity (using only the 300–600 cm$^{-1}$ region) but the values of 0.70 and 0.67 for $^1$6$^+$(*a*) and $^1$6$^+$(*b*), respectively, only serve to highlight the difficulty in differentiating the two spectra. On balance, based primarily on

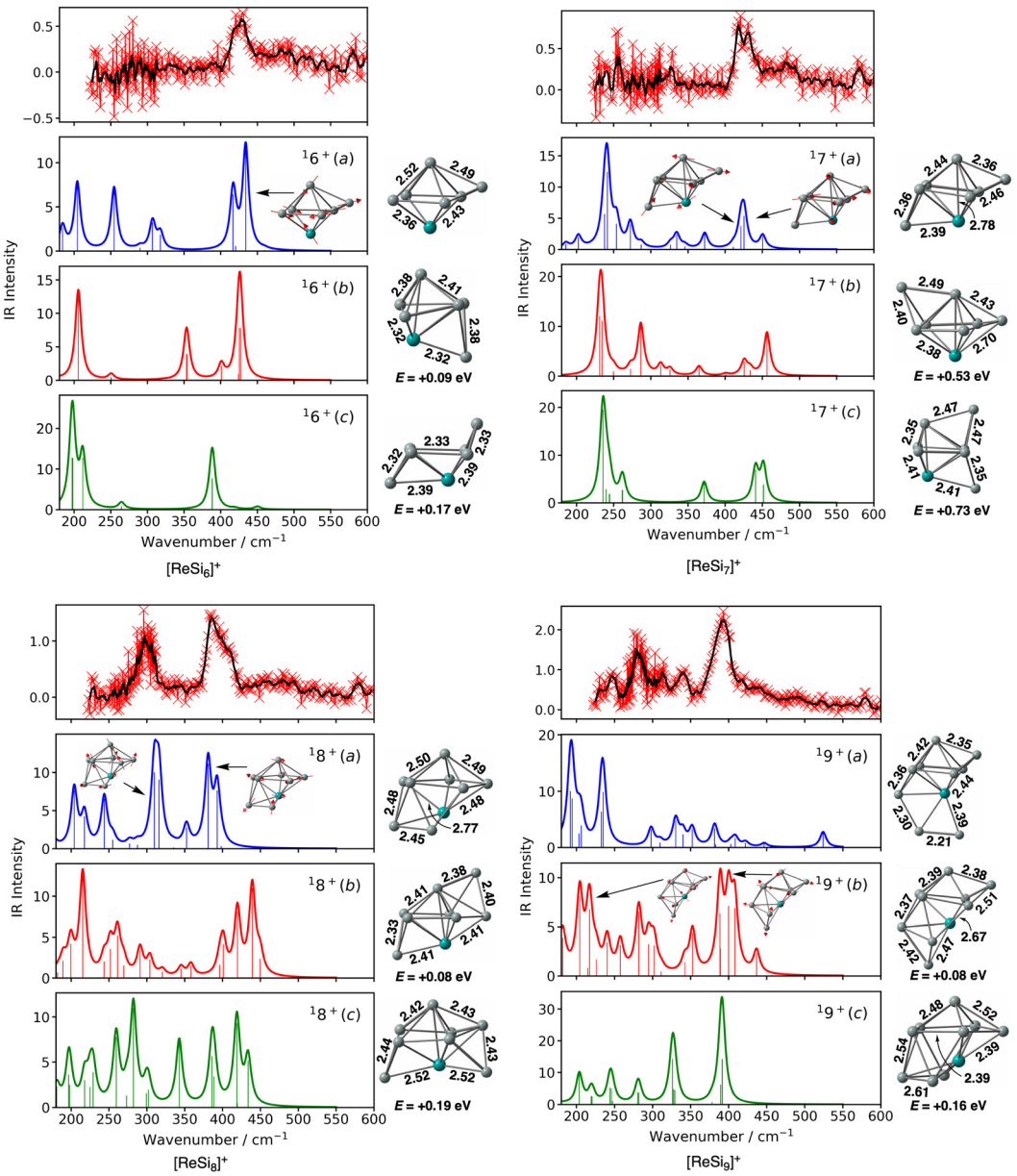


Fig. 5 IR-MPD spectra of $[ReSi_{6-9}]^+$, along with DFT-optimised structures of the singlet ground states and simulated vibrational spectra. Intensity in arbitrary units for the measured spectra, and km mol$^{-1}$ for the computed spectra.

 

its marginally greater stability, we propose $^1$6$^+$($a$) as the most plausible candidate for the structure of $[ReSi_6]^+$, whilst acknowledging that we cannot rule out $^1$6$^+$($b$) as an alternative. We note here that the same structural assignment has been made for $[CoSi_6]^+$ in ref. 39 based on calculations done with the hybrid B3P86 functional.

The difficulties in distinguishing $^1$6$^+$($a$) and $^1$6$^+$($b$) based on their vibrational spectra stem from the fact that the character of the most intense vibrations around 420 cm$^{-1}$ is very similar in both cases. The 416 cm$^{-1}$ ($a''$) and 421 cm$^{-1}$ ($a'$) modes in $^1$6$^+$($a$) can be traced back to the two orthogonal components of the $e$-symmetric 387 cm$^{-1}$ mode of $[ReSi_5]^+$, shifted to higher frequency and split by the presence of the capping Si atom. Similarly, the 425 cm$^{-1}$ band of $^1$6$^+$($b$) (made up of two almost degenerate peaks) can also be traced to the the 387 cm$^{-1}$ mode of the parent octahedron. Given their common heritage, it is perhaps unsurprising that the vibrational fingerprint has only limited capacity to distinguish $^1$6$^+$($a$) from $^1$6$^+$($b$).

The most stable isomer of $[ReSi_7]^+$, $C_s$-symmetric $^1$7$^+$($a$), can be considered, at least conceptually, to be derived either from $^1$6$^+$($a$) by capping a $ReSi_2$ face *trans* to the Si cap, or from $^1$6$^+$($b$) by capping a $Si_3$ face. Alternative growth patterns involving capping a second $Si_3$ faces of $^1$6$^+$($a$) (to give $^1$7$^+$($b$)) or of the $ReSi_2$ face adjacent to the Si cap (to give $^1$7$^+$($c$)) are 0.53 eV and 0.73 eV higher in energy, respectively. The most stable isomer, $^1$7$^+$($a$), also provides a reasonable match to the experimental IR-MPD spectrum, with two almost degenerate modes, $a''$ and $a'$, at 421 and 425 cm$^{-1}$, respectively, coinciding with the measured peak at 430 cm$^{-1}$. The intense 425 cm$^{-1}$ mode of $^1$7$^+$($a$) can again be traced to the 387 cm$^{-1}$ mode of the parent $ReSi_5$ octahedron, and in general the presence of a band in the spectrum around 425 cm$^{-1}$ appears to signal the retention of this octahedral core. The intense $a'$-symmetric mode at 240 cm$^{-1}$, for which there is no obvious match in the experimental spectrum, is the analogue of the 228 cm$^{-1}$ mode in $[ReSi_5]^+$, corresponding to the symmetric Re–$Si_7$ stretch. Its intensity is again substantially reduced when a Xe tag is bound to the Re atom, suggesting that the high intensity is, at least in part, an artifact of the computational model.

The pattern of capping extends through to the largest clusters that we have studied here, $[ReSi_8]^+$ and $[ReSi_9]^+$ (Fig. 5). The most stable isomer of $[ReSi_8]^+$, $^1$8$^+$($a$), is $C_{2v}$ symmetric, and is generated by capping a $ReSi_2$ face of $^1$7$^+$($a$). Alternatively, capping of a $Si_3$ face can generate $^1$8$^+$($b$) while capping a $ReSi_2$ face adjacent to the Si cap generates $^1$8$^+$($c$). All three isomers lie within 0.19 eV of each other, again precluding a confident assignment on energetic grounds alone. The spectrum is, however, somewhat richer, in that a second well-defined and intense low-frequency band around 300 cm$^{-1}$ is present in addition to the now-familiar feature at 420 cm$^{-1}$, and the computed spectrum of $^1$8$^+$($a$) appears most consistent with this pattern, although the differences are again not marked. This conclusion is supported by their rather similar CS scores of 0.71, 0.55 and 0.62 for $^1$8$^+$($a$), $^1$8$^+$($b$) and $^1$8$^+$($c$). The high-frequency region of $^1$8$^+$($a$) is dominated by modes with Re–Si stretching character (381 cm$^{-1}$ and 393 cm$^{-1}$), while the 300 cm$^{-1}$ region contains modes related to the deformation of the Si framework, with little amplitude along the Re–Si bonds.

Finally, $[ReSi_9]^+$ also has three closely-spaced isomers, $^1$9$^+$($a$), $^1$9$^+$($b$) and $^1$9$^+$($c$), all of which lie within 0.16 eV. $^1$9$^+$($a$) offers an obviously poor match to experiment, with no intense bands around 400 cm$^{-1}$, and its cosine similarity (CS = 0.54) to the experimental spectrum is the lowest of the three. Conversely, isomer $^1$9$^+$($b$), derived from $^1$8$^+$($a$) by capping of a $ReSi_2$ face, offers the best match to the experiment (CS = 0.89). The spectrum is now complex, but the absorptions around 400 cm$^{-1}$ are again dominated by Re–Si stretching modes while the lower-frequency region is localised largely on the $Si_n$ framework, much like the 310 cm$^{-1}$ and 316 cm$^{-1}$ peaks in $^1$8$^+$($a$). The emergence of well-resolved features around 300 cm$^{-1}$ appears to be the signature of the growing $Si_n$ skeleton in the larger clusters, $[ReSi_8]^+$ and $[ReSi_9]^+$, which begins to resemble a fragment of a deltahedral cage.

## Patterns of growth

With assignments of the equilibrium structures of the seven $[ReSi_n]^+$ clusters in place, we can now consider the overall pattern of growth. It is useful in this context to consider possible end points for the growth of the cluster, corresponding to complete encapsulation of the Re centre. Fig. 6 illustrates the relationship between the optimised structures of the various clusters considered in the previous sections and a putative $T_d$-symmetric $ReSi_{16}$ Frank–Kasper polyhedron, a structure that has been proposed for $[TaSi_{16}]^+$ (ref. 40) and $[VSi_{16}]^+$.[41] The growth sequence can be divided into an early phase, connecting

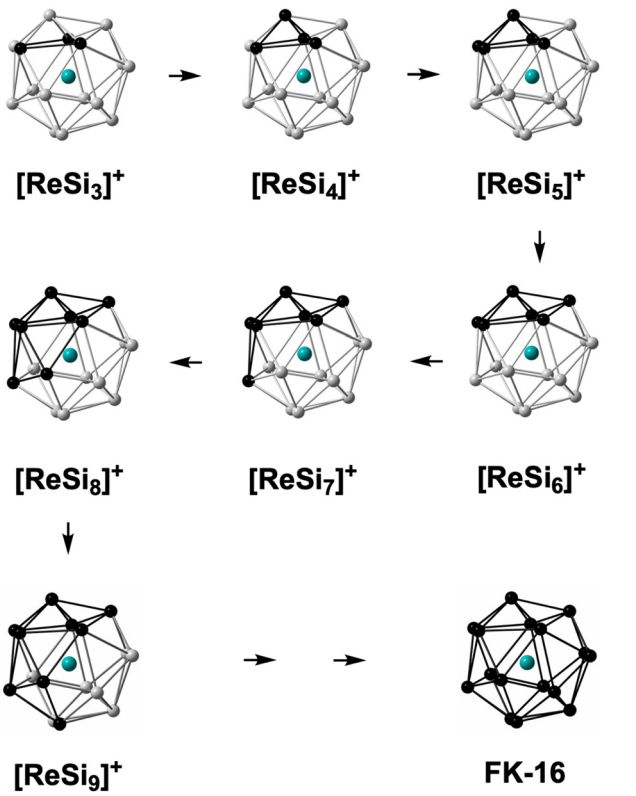


Fig. 6 Growth pattern for the cluster series $[ReSi_n]^+$, $n$ = 3–9, with minimum-energy structures represented as fragments of the 16-vertex Frank–Kasper polyhedron.

tetrahedral $[ReSi_3]^+$ with octahedral $[ReSi_5]^+$, and a later phase, where successive capping of the faces of the octahedron leads to the deltahedral $Si_n$ fragments in $[ReSi_6]^+$, $[ReSi_7]^+$, $[ReSi_8]^+$ and $[ReSi_9]^+$. We emphasise that our choice of the Frank–Kasper polyhedron as the end point in Fig. 6 is not unique, and we could equally have used a 12-vertex icosahedron or indeed approximately spherical 13-14 or 15-vertex polyhedra, as illustrated in Fig. S3 (ESI†). The important point is that the $[ReSi_n]^+$ clusters represent growth towards a limiting 3-dimensional arrangement of Si atoms around the encapsulated Re, rather than a 2-dimensional network. Perhaps unsurprisingly, there is a high degree of convergence between the structural chemistry of the $[ReSi_n]^+$ series and $WSi_n$, $n$ = 6–9 reported by Khanna, Reber and co-workers using the same PBE functional.[42] Their reported global minima for $WSi_7$, $WSi_8$ and $WSi_9$ correspond exactly to those of the isoelectronic $[ReSi_n]^+$ clusters reported in Fig. 6. Even their reported structure of $WSi_6$ differs only very marginally from our $^16^+(a)$ in so much as the capping Si atom shown in Fig. 5 is shifted downwards into the plane to form a mono-capped pentagon.

The construction of a fragment of a larger polyhedron around the central metal ion for $[ReSi_n]^+$ offers a sharp contrast to the corresponding growth pathway for $[MnSi_n]^+$.[10,17] The smaller Mn clusters ($[MnSi_7]^+ \rightarrow [MnSi_{10}]^+$) are all spin quintets and all contain a relatively low coordinate Mn atom/ion bound externally to the surface of a growing $Si_n$ cluster. Only for clusters with more than 10 Si atoms does the Mn ion move to an endohedrally encapsulated position, where it is bound to several of the Si atoms. Similar patterns emerge in the IRMPD study of neutral $MnSi_n$ and $VSi_n$ clusters, where the transition metal is also exohedrally bound to a 3-dimensional $Si_n$ cluster.[21] The majority of these first-row transition metal ions have non-singlet spin states, and it is striking that their structural characteristics converge with those of $[ReSi_n]^+$ only in the rare cases where the multiplicity is low, as for example in $VSi_7$ (a doublet analogous to $^17^+(a)$) and $VSi_8$ (a doublet, analogous to $^18^+(a)$). The contrast between the elements of the first transition series (Mn, V) and the third (Re, W) reflects the rather contracted nature of the 3d orbital, which favours high-spin configurations through the large exchange energies and also limits the extent of covalent interactions with the growing $Si_n$ unit.

## Conclusions

The IR-MPD spectra of $[ReSi_n]^+$·Xe clusters with $n$ in the range 3–9 show trends consistent with the progressive growth towards a limiting Frank–Kasper $ReSi_{16}$ geometry. The spectra of all clusters show an intense feature around 400 $cm^{-1}$ corresponding to vibrations of the Re–Si bonds, and transitions around 300 $cm^{-1}$ corresponding to Si–Si stretches which become relatively more intense as the clusters increase in size. In the smaller clusters such as $[ReSi_3]^+$ and $[ReSi_5]^+$, high point symmetry leads to a relatively simple spectrum dominated by a single intense band, but the number of bands increases with size of cluster, to the point where it becomes difficult to distinguish between almost degenerate isomers that differ only in the position of one or two Si atoms. The different patterns followed by the iso-electronic Re and Mn clusters can be traced to the relative accessibility of the 5d orbitals, which facilitates formation of a more open pseudo 2-dimensional network of Si atoms.

## Author contributions

Conceptualisation: PC, AF, EJ, JEM and PL. Software: RS. Investigation: PC and Dr Philipp Gruene. Methodology: PC, AF, EJ, PL. Writing – original draft: RS. Formal analysis: RS. Supervision: EJ, JEM, PL. Writing – review and editing: RS, PC, AF, EJ, JEM, PL. Supervision: EJ, JEM and PL. Funding acquisition: EJ, JEM and PL.

## Data availability

The datasets supporting this article have been uploaded as part of the ESI.†

## Conflicts of interest

There are no conflicts to declare.

## Acknowledgements

RS acknowledges the EPSRC (UK) for a studentship through the DTP scheme (EP/W524311/1). The experimental work was supported by the KU Leuven Research Council (C1 Grant C14/22/103) and by the Research Foundation Flanders (FWO G033724N). The authors gratefully acknowledge the Nederlandse Organisatie voor Wetenschappelijk Onderzoek (NWO) for the support of the FELIX Laboratory and thank the FELIX staff.

## Notes and references

1 W. D. Knight, K. Clemenger, W. A. de Heer, W. A. Saunders, M. Y. Chou and M. L. Cohen, *Phys. Rev. Lett.*, 1984, **52**, 2141–2143.
2 Z. Lin, T. Slee and D. Mingos, *Chem. Phys.*, 1990, **142**, 321–334.
3 K. Wade, *J. Chem. Soc. D*, 1971, 792–793.
4 E. D. Jemmis, M. M. Balakrishnarajan and P. D. Pancharatna, *J. Am. Chem. Soc.*, 2001, **123**, 4313–4323.
5 S. Mitzinger, L. Broeckaert, W. Massa, F. Weigend and S. Dehnen, *Nat. Commun.*, 2016, **7**, 10480.
6 J. E. McGrady, F. Weigend and S. Dehnen, *Chem. Soc. Rev.*, 2022, **51**, 628–649.
7 Y. Wang, J. E. McGrady and Z.-M. Sun, *Acc. Chem. Res.*, 2021, **54**, 1506–1516.
8 A. Fielicke, G. von Helden and G. Meijer, *Eur. Phys. J. D*, 2005, **34**, 83–88.
9 V. T. Ngan, P. Gruene, P. Claes, E. Janssens, A. Fielicke, M. T. Nguyen and P. Lievens, *J. Am. Chem. Soc.*, 2010, **132**, 15589–15602.
10 V. T. Ngan, E. Janssens, P. Claes, J. T. Lyon, A. Fielicke, M. T. Nguyen and P. Lievens, *Chem. – Eur. J.*, 2012, **18**, 15788–15793.

 

11 P. Claes, V. T. Ngan, M. Haertelt, J. T. Lyon, A. Fielicke, M. T. Nguyen, P. Lievens and E. Janssens, *J. Chem. Phys.*, 2013, **138**, 194301.
12 B. Yang, X.-L. Xu, H.-G. Xu, U. Farooq and W.-J. Zheng, *Phys. Chem. Chem. Phys.*, 2019, **21**, 6207–6215.
13 X. Liang, X. Kong, S.-J. Lu, Y. Huang, J. Zhao, H.-G. Xu, W. Zheng and X. C. Zeng, *J. Phys.: Condens.Matter*, 2018, **30**, 335501.
14 X.-Q. Liang, X.-J. Deng, S.-J. Lu, X.-M. Huang, J.-J. Zhao, H.-G. Xu, W.-J. Zheng and X. C. Zeng, *J. Phys. Chem. C*, 2017, **121**, 7037–7046.
15 J. Bai, L.-F. Cui, J. Wang, S. Yoo, X. Li, J. Jellinek, C. Koehler, T. Frauenheim, L.-S. Wang and X. C. Zeng, *J. Phys. Chem. A*, 2006, **110**, 908–912.
16 S. Furuse, K. Koyasu, J. Atobe and A. Nakajima, *J. Chem. Phys.*, 2008, **129**, 064311.
17 V. Zamudio-Bayer, L. Leppert, K. Hirsch, A. Langenberg, J. Rittmann, M. Kossick, M. Vogel, R. Richter, A. Terasaki, T. Möller, B. V. Issendorff, S. Kümmel and J. T. Lau, *Phys. Rev. B: Condens. Matter Mater. Phys.*, 2013, **88**, 115425.
18 S. N. Khanna, B. K. Rao and P. Jena, *Phys. Rev. Lett.*, 2002, **89**, 016803.
19 V. Arcisauskaite, D. Fijan, M. Spivak, C. D. Graaf and J. E. McGrady, *Phys. Chem. Chem. Phys.*, 2016, **18**, 24006–24014.
20 V. T. Ngan, K. Pierloot and M. T. Nguyen, *Phys. Chem. Chem. Phys.*, 2013, **15**, 5493–5498.
21 P. Claes, V. T. Ngan, M. Haertelt, J. T. Lyon, A. Fielecke, M. T. Nguyen, P. Lievens and E. Janssens, *J. Chem. Phys.*, 2013, **138**, 194301.
22 H. Hiura, T. Miyazaki and T. Kanayama, *Phys. Rev. Lett.*, 2001, **86**, 1733–1736.
23 J.-G. Han, Z.-Y. Ren and B.-Z. Lu, *J. Phys. Chem. A*, 2004, **108**, 5100–5110.
24 D. Oepts, A. van der Meer and P. van Amersfoort, *Infrared Phys. Technol.*, 1995, **36**, 297–308.
25 P. Ferrari, J. Vanbuel, Y. Li, T.-W. Liao, E. Janssens and P. Lievens, *The Double-Laser Ablation Source Approach*, John Wiley & Sons, Ltd, Weinheim, 2017, ch. 4, pp. 59–78.
26 J. Lv, Y. Wang, L. Zhu and Y. Ma, *J. Chem. Phys.*, 2012, **137**, 084104.
27 U. Farooq, S. Naz, H.-G. Xu, B. Yang, X.-L. Xu and W.-J. Zheng, *Coord. Chem. Rev.*, 2020, **403**, 213095.
28 J. P. Perdew, K. Burke and M. Ernzerhof, *Phys. Rev. Lett.*, 1996, **77**, 3865–3868.
29 L. E. Roy, P. J. Hay and R. L. Martin, *J. Chem. Theory Comput.*, 2008, **4**, 1029–1031.
30 M. J. Frisch, G. W. Trucks, H. B. Schlegel, G. E. Scuseria, M. A. Robb, J. R. Cheeseman, G. Scalmani, V. Barone, G. A. Petersson, H. Nakatsuji, M. C. X. Li, A. Marenich, J. Bloino, B. G. Janesko, R. Gomperts, B. Mennucci, H. P. Hratchian, J. V. Ortiz, A. F. Izmaylov, J. L. Sonnenberg, D. Williams-Young, F. Ding, F. Lipparini, F. Egidi, J. Goings, B. Peng, A. Petrone, T. Henderson, D. Ranasinghe, V. G. Zakrzewski, J. Gao, N. Rega, G. Zheng, W. Liang, M. Hada, M. Ehara, K. Toyota, R. Fukuda, J. Hasegawa, M. Ishida, T. Nakajima, Y. Honda, O. Kitao, H. Nakai, T. Vreven, K. Throssell, J. A. Montgomery, Jr., J. E. Peralta, F. Ogliaro, M. Bearpark, J. J. Heyd, E. Brothers, K. N. Kudin, V. N. Staroverov, T. Keith, R. Kobayashi, J. Normand, K. Raghavachari, A. Rendell, J. C. Burant, S. S. Iyengar, J. Tomasi, M. Cossi, J. M. Millam, M. Klene, C. Adamo, R. Cammi, J. W. Ochterski, R. L. Martin, K. Morokuma, O. Farkas, J. B. Foresman and D. J. Fox, *Gaussian09*, 2009.
31 E. V. Lenthe and E. J. Baerends, *J. Comput. Chem.*, 2012, **24**, 1142–1156.
32 G. te Velde, F. M. Bickelhaupt, E. J. Baerends, C. F. Guerra, S. J. A. van Gisbergen, J. G. Snijders and T. Ziegler, *J. Comput. Chem.*, 2001, **22**, 931–967.
33 V. Khanna, R. Singh, P. Claes, M. T. Nguyen, A. Fielicke, E. Janssens, P. Lievens and J. E. McGrady, *J. Phys. Chem. A*, 2022, **126**, 1617–1626.
34 J. Xu, J. M. Bakker, O. V. Lushchikova, P. Lievens, E. Janssens and G.-L. Hou, *J. Am. Chem. Soc.*, 2023, **145**, 22243–22251.
35 W. Fu and W. S. Hopkins, *J. Phys. Chem. A*, 2018, **122**, 167–171.
36 V. T. Ngan, E. Janssens, P. Claes, A. Fielicke, M. T. Nguyen and P. Lievens, *Phys. Chem. Chem. Phys.*, 2015, **17**, 17584–17591.
37 M. Yamaguchi, S. Kudoh, K. Miyajima, O. V. Lushchikova, J. M. Bakker and F. Mafuné, *J. Phys. Chem. C*, 2019, **123**, 3476–3481.
38 C. Kerpal, D. J. Harding, A. C. Hermes, G. Meijer, S. R. Mackenzie and A. Fielicke, *J. Phys. Chem. A*, 2013, **117**, 1233–1239.
39 Y. Li, N. M. Tam, A. P. Woodham, J. T. Lyon, Z. Li, P. Lievens, A. Fielicke, M. T. Nguyen and E. Janssens, *J. Phys. Chem. C*, 2016, **120**, 19454–19460.
40 M. Nakaya, T. Iwasa, H. Tsunoyama, T. Eguchi and A. Nakajima, *Nanoscale*, 2014, **6**, 14702–14707.
41 P. Claes, E. Janssens, V. Ngan, P. Gruene, J. Lyon, D. Harding, A. Fielicke, M. Nguyen and P. Lievens, *Phys. Rev. Lett.*, 2011, **107**, 173401.
42 M. B. Abreu, A. C. Reber and S. N. Khanna, *J. Chem. Phys.*, 2015, **143**, 074310.